^{14}C(^{11}B,^{10}B)^{15}C REACTION at $E_{\rm lab}$ = 45 MeV AND THE ^{10}B+^{15}C OPTICAL POTENTIAL

S.Yu. Mezhevych[a], A.T. Rudchik[a], A.A. Rudchik[a]
K.W. Kemper[b], K. Rusek[c], O.A. Ponkratenko[a]
E.I. Koshchy[d], S.B. Sakuta[e]

[a]Institute for Nuclear Research, Ukrainian Academy of Sciences
Prospect Nauki 47, 03680 Kyiv, Ukraine
[b]Physics Department, Florida State University
Tallahassee, FL 32306-4350, USA
[c]Heavy Ion Laboratory, University of Warsaw
L. Pasteura 5A, 02-093 Warsaw, Poland
[d]Cyclotron Institute Texas A&M University
College Station, TX 77843, USA
[e]Russian Research Center "Kurchatov Institut"
Kurchatov Sq. 1, 123182 Moscow, Russia

(Received November 9, 2020; accepted February 5, 2021)

Complete angular distributions including both forward and backward angles are reported for the ^{14}C(^{11}B,^{10}B)^{15}C reaction at $E_{\rm lab}$(^{11}B) = 45 MeV for the ground and excited states of ^{10}B and ^{15}C. The experimental data were analyzed within the coupled reaction channels method that included the ^{11}B+^{14}C elastic scattering channel as well as channels for one- and two-step transfers of nucleons in the coupling scheme. The necessary ^{11}B+^{14}C optical potential parameters were obtained from previous work, while those for ^{10}B+^{15}C were deduced from fitting the CRC reaction calculations to the ^{14}C(^{11}B,^{10}B)^{15}C reaction data. Needed spectroscopic amplitudes of transferred nucleons and clusters were calculated within the translational-invariant shell model. The data are well described by neutron transfers, while contributions from two-step transfers were found to be negligible. Recently published global optical potentials for the elastic scattering of the ^{8,10,11}B isotopes were tested as part of the analysis and found to satisfactorily describe this reaction data if the surface imaginary potentials were omitted for both the entrance and the exit channels, and the parameters for volume real and imaginary potentials were slightly modified.

DOI:10.5506/APhysPolB.52.109

1. Introduction

The investigation of properties of short-lived neutron-rich nuclei, such as ^{15}C, can be performed either in direct experiments with ^{15}C produced as secondary ion beams, or ^{15}C produced as a product in an exit reaction channel. Since production of radioactive ^{15}C ion beams is still a difficult task [1], only a limited number of direct experiments have been performed to date with secondary ^{15}C ion beams. Recent examples are two-neutron removal cross sections [2] from ^{15,16}C to verify the odd–even staggering of two neutron removal cross sections in the carbon isotopes and the study of the excited states of ^{14}B via the ^{15}C(d,^{3}He)^{14}B reaction performed in inverse kinematics [3].

The spectroscopy of ^{15}C states was probed in the ^{12}C(^{12}C,^{9}C)^{15}C reaction [4], resulting in several new excited states of ^{15}C being observed. In [5], the ^{13}C(^{14}C,^{15}C)^{12}C and $d(^{14}\mathrm{C},p)^{15}$C reactions were used to extract asymptotic normalization coefficients and spectroscopic factors for the ^{14}C+n $\rightarrow$^{15}C system to give information for further estimation of the ^{14}C$(n,\gamma)^{15}$C reaction rates in the stellar environment. In other studies [6, 7], the (d,p) reactions at different energies were employed to extract the asymptotic normalization coefficients and spectroscopic factors for the ground and first excited states of ^{15}C, while the neutron halo properties of ^{15}C were investigated in a recent work [8], where results of various calculations were compared with the available experimental data. The ^{13}C(^{18}O,^{16}O)^{15}C reaction at $E = 84$ MeV was used [9, 10] to explore a microscopic description of two-neutron transfers populating the ground and excited states of ^{15}C.

The purpose of the present work is to deduce the parameters of an optical model (OM) potential from the final-state interaction of the ^{10}B+^{15}C nuclei produced in the ^{14}C(^{11}B,^{10}B)^{15}C reaction at $E_{\mathrm{lab}}(^{11}\mathrm{B}) = 45$ MeV, as well as to investigate the differences (isotopic effects) of OM potentials deduced for the ^{10}B+^{13}C [11] and ^{10}B+^{12}C [12] interacting systems. Another goal is to investigate whether sequential transfer of a proton and/or a deuteron can compete with direct transfer of a neutron in this reaction, since large values of spectroscopic amplitudes are generated in the framework of the translational-invariant shell model for $^{14}\mathrm{C} \rightarrow {}^{13}\mathrm{B} + p$, $^{12}\mathrm{C} \rightarrow {}^{11}\mathrm{B} + p$ and $^{12}\mathrm{C} \rightarrow {}^{10}\mathrm{B} + d$ vertices in the diagram for $p + d$ transfer in this reaction. Finally, the obtained experimental data for the ^{14}C(^{11}B,^{10}B)^{15}C reaction at $E_{\mathrm{lab}}(^{11}\mathrm{B}) = 45$ MeV allow the testing of recently published global OM potentials for ^{8,10,11}B projectiles [13], through their use as parameters needed to carry out the coupled reaction channels (CRC) calculations for this reaction.

The paper is organized as follows. Section 2 contains a brief description of the experimental method, Section 3 — the procedure for the CRC calculations, tables with the deduced optical potential parameters for the entrance $^{14}C+^{11}B$ and exit $^{15}C+^{10}B$ channels, the spectroscopic amplitudes of the transferred nucleons and clusters, and the results of the reaction analysis. The last section provides the summary of this work.

2. Experimental procedure

Angular distributions for $^{14}C(^{11}B, X)$ scattering and transfer reactions were measured simultaneously at an energy $E_{lab}(^{11}B) = 45$ MeV using the ^{11}B beam from the Warsaw University cyclotron U-200P. The same experimental system described in [14, 15], with the analysis as carried out previously for the $^{13}C(^{11}B,^{12}C)^{12}B$ reaction [16], was used in this work so will not be repeated here. The obtained typical energy spectra of the $^{14}C(^{11}B,^{10}B)^{15}C$ reaction products ^{10}B and ^{15}C are shown in Fig. 1 (a), (b), respectively, after subtraction of multi-particle reaction backgrounds and overlaps from the neighboring sub-loci of ^{11}B and ^{14}C isotopes. These residual energy spectra were fitted by symmetric Gaussian functions (code PEAKFIT) with the extracted peak areas used to determine the cross sections for the $^{14}C(^{11}B,^{10}B)^{15}C$ reaction at $\theta_{cm}(^{10}B)$ angles from the ^{10}B spectra and at $\theta_{cm}(^{10}B) = 180° - \theta_{cm}(^{15}C)$ angles from the ^{15}C spectra. The same procedure as in [16] was used to minimize the contributions from residual

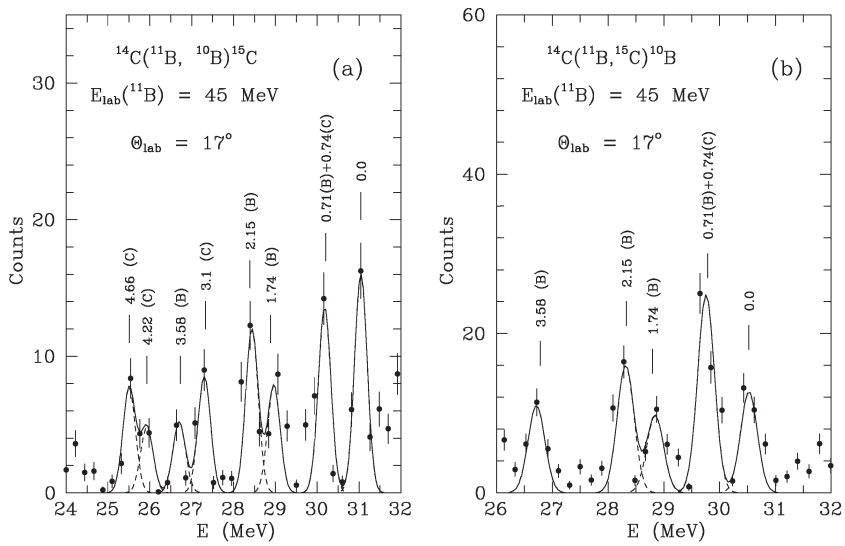

Fig. 1. Typical energy spectra of ^{10}B (a) and ^{15}C (b) from the $^{14}C(^{11}B,^{10}B)^{15}C$ reaction at the energy of $E_{lab}(^{11}B) = 45$ MeV (curves show the Gauss symmetric fitted forms).

backgrounds observed in the energy spectra. The area errors of the peaks were estimated to be about 20%, if the peaks were well resolved and 30–40% for poorly resolved peaks.

The normalization factor, necessary to obtain the absolute cross section of the ^{14}C(^{11}B,^{10}B)^{15}C reaction, was the same as that used in the previous work of the elastic and inelastic scattering of ^{11}B by ^{14}C [15], measured in the same experiment. The overall absolute error was estimated to be less than 20%.

3. Analysis of the reaction data

The ^{14}C(^{11}B,^{10}B)^{15}C experimental data were analyzed within the CRC method. The ^{14}C+^{11}B elastic scattering, including reorientation of the ^{11}B [15], as well as transfer reactions as shown by diagrams in Fig. 2, were included in the channel coupling scheme. Standard Woods–Saxon (WS) optical potentials were used in entrance and exit channels of the calculations and their form, given here for completeness, is:

$$U(r) = -V_0 \left[1 + \exp\left(\frac{r - R_V}{a_V}\right)\right]^{-1} - iW_S \left[1 + \exp\left(\frac{r - R_W}{a_W}\right)\right]^{-1} \quad (1)$$

with the Coulomb potential being that for uniformly charged spheres

$$V_{\rm C}(r) = \begin{cases} \frac{Z_{\rm P} Z_{\rm T} e^2}{2R_C}\left(3 - \frac{r^2}{R_C^2}\right), & r \le R_C \\ \frac{Z_{\rm P} Z_{\rm T} e^2}{r}, & r > R_C \end{cases}. \quad (2)$$

Here, the form of the radii is given by

$$R_i = r_i \left(A_{\rm P}^{1/3} + A_{\rm T}^{1/3}\right), \qquad i = V, W, C, \quad (3)$$

where $A_{\rm P}$, $A_{\rm T}$ and $Z_{\rm P}$, $Z_{\rm T}$ are the mass and charge numbers of ^{11}B, ^{14}C (entrance channel) and ^{15}C, ^{10}B (exit channel). The parameter $r_C = 1.25$ fm was used in all the calculations.

The wave function of x for a nucleus $A = C + x$ was calculated by varying the depth of the WS binding potential to reproduce the binding energy of nucleus A. The geometry parameters of the cluster binding potentials were the following: $a = 0.65$ fm and $r_0 = 1.25A^{1/3}/(C^{1/3} + x^{1/3})$ fm.

The spectroscopic amplitudes S_x of clusters x for the nuclear systems $A = C + x$, used in the CRC calculations for the transfer reactions were obtained within the translational-invariant shell model (TISM) [17] using the computer code DESNA [18, 19] and Boyarkina's wave function tables for 1p-shell nuclei [20]. The calculated values of the amplitudes S_x are listed in Table I.

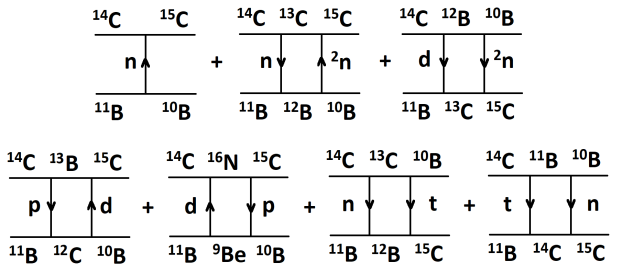

Fig. 2. Diagrams of different ^{14}C(^{11}B,^{10}B)^{15}C reaction mechanisms.

TABLE I

Spectroscopic amplitudes S_x of x-clusters in $A = C + x$ systems.

A	C	x	nL_j	S_x	A	C	x	nL_j	S_x
^{10}B	^{9}Be	p	$1P_{3/2}$	1.185	^{13}C	^{10}B	t	$1F_{5/2}$	0.108[a]
^{10}B$^*_{0.72}$	^{9}Be	p	$1P_{1/2}$	−0.361[a]				$1F_{7/2}$	0.747
			$1P_{3/2}$	−0.323	^{13}C	^{10}B$^*_{0.72}$	t	$2P_{1/2}$	−0.655[a]
^{10}B$^*_{1.74}$	^{9}Be	p	$1P_{3/2}$	0.994[a]				$2P_{3/2}$	0.231
^{10}B$^*_{2.15}$	^{9}Be	p	$1P_{1/2}$	−0.663[a]	^{13}C	^{10}B$^*_{1.74}$	t	$2P_{1/2}$	−0.120
			$1P_{3/2}$	0.741	^{13}C	^{10}B$^*_{2.15}$	t	$2P_{1/2}$	−0.069[a]
^{10}B$^*_{3.59}$	^{9}Be	p	$1P_{1/2}$	0.838				$2P_{3/2}$	−0.196
^{11}B	^{9}Be	d	$2S_1$	−0.607[a]	^{13}C	^{10}B$^*_{3.59}$	t	$2P_{3/2}$	−0.694[a]
			$1D_1$	−0.109[a]				$1F_{5/2}$	0.404
			$1D_3$	0.610[a]	^{13}C	^{11}B	d	$2S_1$	−0.263
^{11}B	^{10}B	n	$1P_{3/2}$	−1.347[a]				$1D_1$	−0.162
^{11}B	^{10}B$^*_{0.72}$	n	$1P_{1/2}$	−0.268				$1D_2$	−0.485[a]
			$1P_{3/2}$	0.240[a]	^{14}C	^{11}B	t	$2P_{3/2}$	−0.368[a]
^{11}B	^{10}B$^*_{1.74}$	n	$1P_{3/2}$	−0.494	^{14}C	^{12}B	d	$1D_1$	−1.010
^{11}B	^{10}B$^*_{2.15}$	n	$1P_{1/2}$	−0.571	^{14}C	^{13}B	p	$1P_{3/2}$	1.695[a]
			$1P_{3/2}$	−0.638[a]	^{14}C	^{13}C	n	$1P_{1/2}$	−1.094[a]
^{11}B	^{10}B$^*_{3.59}$	n	$1P_{1/2}$	−0.805[a]	^{15}C	^{12}B	t	$3S_{1/2}$	−0.160[a]
^{12}B	^{10}B	^2n	$1D_2$	−0.152				$2D_{3/2}$	0.057
^{12}B	^{10}B$^*_{0.72}$	^2n	$2S_0$	−0.746	^{15}C	^{13}B	d	$2P_1$	−0.144
			$1D_2$	−0.046				$1F_2$	−0.338[a]
^{12}B	^{10}B$^*_{2.15}$	^2n	$1D_2$	−0.380	^{15}C$^*_{0.74}$	^{13}B	d	$2P_1$	0.343
^{12}B	^{10}B$^*_{3.59}$	^2n	$1D_2$	0.060[a]				$2P_2$	0.279[a]
^{12}B	^{11}B	n	$1P_{1/2}$	−0.142				$1F_3$	0.100
			$1P_{3/2}$	−0.127[a]	^{15}C	^{14}C	n	$2S_{1/2}$	−0.882
^{12}C	^{10}B	d	$1D_3$	1.780	^{15}C$^*_{0.74}$	^{14}C	n	$1D_{5/2}$	−0.882
^{12}C	^{10}B$^*_{0.72}$	d	$1D_1$	1.165	^{16}N	^{14}C	d	$2P_2$	0.380
^{12}C	^{10}B$^*_{2.15}$	d	$2S_1$	−1.386	^{16}N	^{15}C	p	$1P_{3/2}$	0.500
^{12}C	^{10}B$^*_{3.59}$	d	$1D_2$	1.504	^{16}N	^{15}C$^*_{0.74}$	p	$1P_{1/2}$	0.238[a]
^{12}C	^{11}B	p	$1P_{3/2}$	−1.706[a]				$1P_{3/2}$	−0.318

[a] $S_{\mathrm{FRESCO}} = (-1)^{J_C+j-J_A} S_x = -S_x$.

The calculations were performed with the code FRESCO [21]. For the entrance ^{11}B+^{14}C channel, the WS potential parameters were taken from [15], in which the elastic and inelastic scattering of these nuclei was investigated. The parameters of the WS potential for the ^{10}B+^{15}C interaction were deduced from fitting the calculated cross sections to the ^{14}C(^{11}B,^{10}B)^{15}C experimental data and they are listed in Table II.

TABLE II

Parameters of WS optical potentials.

T+P	$E_{\rm cm}$ [MeV]	V_0 [MeV]	r_V [fm]	a_V [fm]	W_S [MeV]	r_W [fm]	a_W [fm]	Ref.
^{14}C+^{11}B	25.2	266.6	0.750	0.740	7.5	1.345	0.740	[15]
^{15}C+^{10}B	14.96	174.0	0.791	0.780	9.0	0.970	0.650	This work
^{13}C+^{10}B	10.2–26	66.85	1.094	0.609	10.0	1.200	0.700	[11]
^{12}C+^{10}B	22.53	100.0	1.150	0.428	15.0	1.300	0.248	[12]

Comparing with the ^{10}B+^{12}C OM potential obtained at slightly higher energy [12], the real part of ^{15}C potential is much more diffuse at the surface. Its imaginary part is also more diffuse than the one for ^{12}C. These differences may be related to the weakly bound structure of ^{15}C [8].

Angular distributions of the ^{14}C(^{11}B,^{10}B)^{15}C reaction at $E_{\rm lab}(^{11}{\rm B}) = 45$ MeV for the ground states of ^{15}C and ^{10}B are shown in Fig. 3 together with CRC calculations for different transfer reactions. The cross sections for the two-step transfers of $p+d$ and $d+p$ (curve $\langle pd\rangle$ in Fig. 3, coherent sum) are about 1–2 orders of magnitude lower than the cross sections for the direct transfer of a neutron (curve $\langle n\rangle$) despite the fact that large values of spectroscopic amplitudes were generated in the framework of TISM for $^{14}{\rm C}\to{}^{13}{\rm B}+p$, $^{12}{\rm C}\to{}^{11}{\rm B}+p$ and $^{12}{\rm C}\to{}^{10}{\rm B}+d$ vertices in the diagram for proton + deuteron transfer (Fig. 2, see also Table I). Contributions of other two-step transfer reactions as $n+{}^2n$ (curve $\langle n^2n\rangle$), $d+{}^2n$ (curve $\langle d^2n\rangle$), $n+t$ and $t+n$ (curve $\langle nt\rangle$), shown in Fig. 3 by the respective curves, were also found to be negligible. Thus, the reaction is dominated by the single neutron transfer over the full angular range of the data.

In Fig. 4, we show the comparison of cross sections for one-step neutron transfer in the ^{14}C(^{11}B,^{10}B)^{15}C reaction, calculated using the OM parameters obtained in this work for the ^{15}C+^{10}B interaction, and previously obtained parameters for ^{10}B+^{13}C [11] and ^{10}B+^{12}C [12] interactions (see Table II). The observed differences in the calculated cross sections (so-called isotopic effects) may be caused by the different structures as well as different transfer Q-values of the ^{12}C, ^{13}C and ^{15}C isotopes interacting with ^{10}B

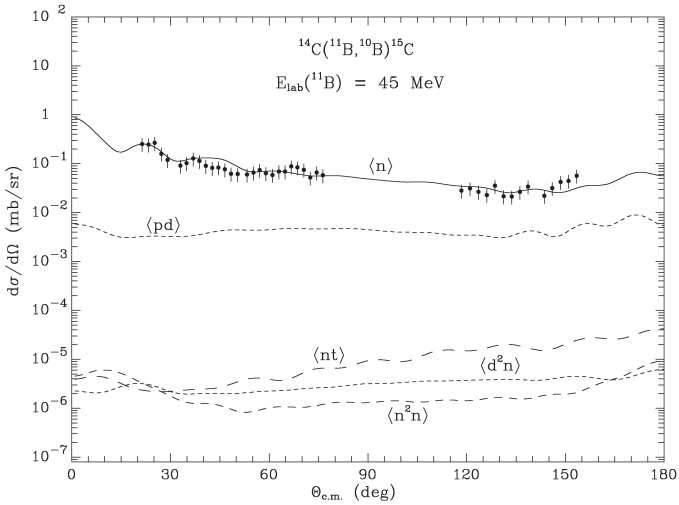

Fig. 3. Angular distributions of the $^{14}C(^{11}B,^{10}B)^{15}C$ reaction at the energy of $E_{lab}(^{11}B) = 45$ MeV for the ground states of ^{10}B and ^{15}C. The curves show CRC cross sections calculated with the WS potentials (Table II) for different transfer processes.

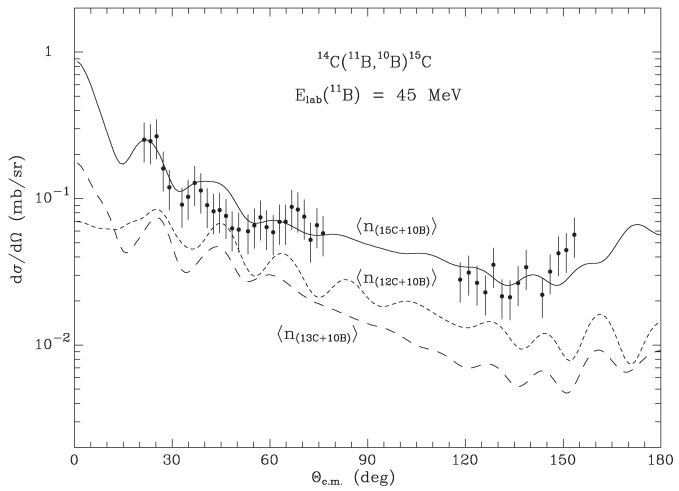

Fig. 4. Angular distributions of the $^{14}C(^{11}B,^{10}B)^{15}C$ reaction at the energy of $E_{lab}(^{11}B) = 45$ MeV for the ground states of ^{10}B and ^{15}C. The curves show CRC calculations with different OM parameters for the ^{10}B+^{15}C interaction (Table II).

nucleus: as ^{12}C is commonly considered to have a negative quadrupole deformation, while that of ^{13}C is rather positive [14, 22], and ^{15}C is known to be a stretched nucleus with halo properties summarized recently [8]. As for the missing calculation with a ^{10}B+^{14}C interaction potential in Fig. 4, we could not find in the literature the experimental data for ^{10}B+^{14}C elastic scattering or this pair of nuclei produced in an exit reaction channel. Thus, in order to fill this gap, we plan to analyze the experimental data for the ^{13}C(^{11}B,^{10}B)^{14}C reaction measured together with the elastic and inelastic scattering at $E_{\rm lab}(^{11}\mathrm{B}) = 45$ MeV [14], to deduce the OM potential parameters for the ^{10}B+^{14}C interaction in the future.

Angular distributions and CRC calculations for the excited states 0.72 MeV (1^+) of ^{10}B and 0.74 MeV ($5/2^+$) of ^{15}C (unresolved in the experiment), and 1.74 MeV (0^+) of ^{10}B are shown in Fig. 5 in the upper and lower panels, respectively. The dashed curves $\langle n - {}^{10}\mathrm{B}^*\rangle$ and $\langle n - {}^{15}\mathrm{C}^*\rangle$ in the upper panel of Fig. 5 show the cross sections for direct transfers of neutrons for the excited states 0.72 MeV (1^+) of ^{10}B and 0.74 MeV ($5/2^+$) of ^{15}C, and curve $\Sigma_{\rm 2st}$ — the incoherent sum of two-step transfer reactions leading to the population of these two states. Note that the transition to the 0.74 MeV ($5/2^+$) of ^{15}C dominates. The solid curve $\langle n\rangle$ in the lower panel of Fig. 5 shows the calculated cross sections for direct transfer of a neutron in the ^{14}C(^{11}B,^{10}B)^{15}C reaction leaving ^{10}B in the excited 1.74 MeV (0^+) state, the curve $\Sigma_{\rm 2st}$ shows the coherent sum of two-step processes for this state.

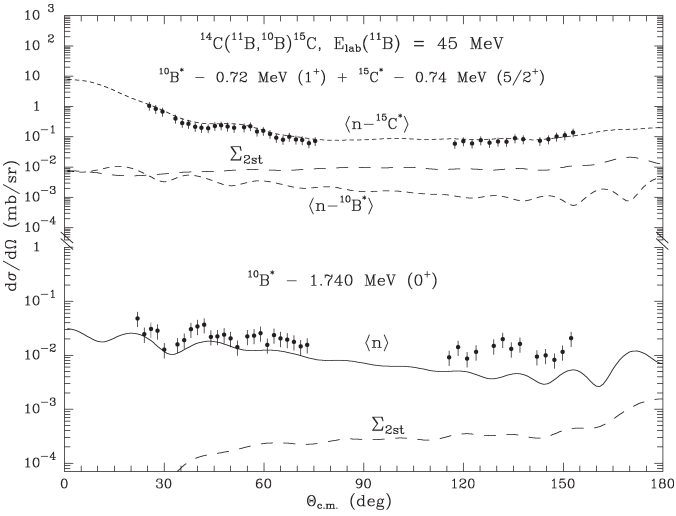

Fig. 5. Angular distributions of the ^{14}C(^{11}B,^{10}B)^{15}C reaction for the excited states 0.72 MeV (1^+) of ^{10}B and 0.74 MeV ($5/2^+$) of ^{15}C (unresolved in the experiment) and 1.74 MeV (0^+) of ^{10}B. The curves show CRC cross sections for different processes (see the text for details).

In the upper panel of Fig. 6, angular distributions of the reaction for transitions to the excited 2.154 MeV (1^+) state of ^{10}B are shown, while that for the excited 3.587 MeV (2^+) state of ^{10}B are placed in the lower panel. Curves $\langle n \rangle$ and Σ_{2st} show contributions of direct neutron transfer and the coherent sum of the two-step processes, respectively.

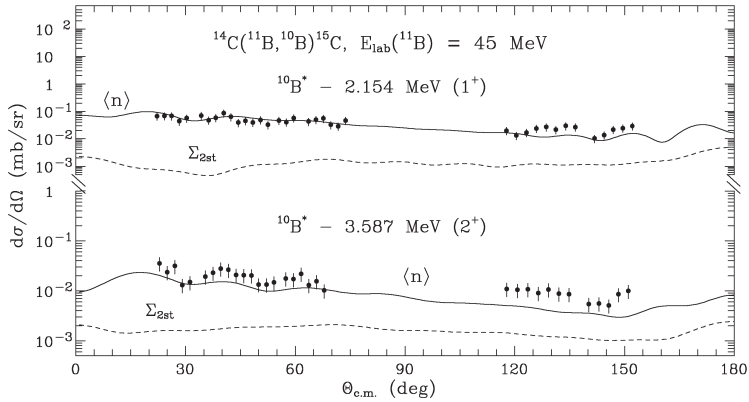

Fig. 6. Angular distributions of the $^{14}C(^{11}B,^{10}B)^{15}C$ reaction for the excited 2.154 MeV (1^+) and 3.587 MeV (2^+) states of ^{10}B. The curves show CRC cross sections for different processes (see the text for details).

As can be seen from Figs. 5–6, the contributions of two-step processes are negligible, as direct transfer of a neutron dominates for all of the above mentioned excited states of ^{10}B in the $^{14}C(^{11}B,^{10}B)^{15}C$ reaction.

In Fig. 7, angular distributions for the exited states of ^{15}C located at energies above the neutron separation energy (1.218 MeV) are shown. Results of CRC calculations for transfer to these resonances will be presented in a separate paper.

The present data leading to the population of the ground states of the both, projectile and target, allow for the test of recently published global optical model potentials (OMP) for ^{8,10,11}B projectiles [13]. The standard global phenomenological OM potential in Ref. [13] is defined by

$$V(r,E) = -V_0(r,E) - i[W_S(r,E) + W_D(r,E)] + V_C(r)\,. \qquad (4)$$

The Coulomb interaction $V_C(r)$ is given by equation (2), the sum of the potentials for the real $V_0(r)$ and imaginary parts for volume absorption $W_S(r)$, adjusted for a given energy E for the interaction of the pair of nuclei, is defined by equation (1), while the surface imaginary potential $W_D(r)$, adjusted for a given energy E for the interaction of the pair of nuclei, is given by the expression

$$W_D(r) = 4W_D \left[\exp\left(\frac{r - R_D}{a_D}\right)\right] \Big/ \left[1 + \exp\left(\frac{r - R_D}{a_D}\right)\right]^2 . \qquad (5)$$

The radii of these potentials are dependent on the target masses only

$$R_i = r_i A_{\mathrm{T}}^{1/3} , \qquad i = V, W, D, C . \qquad (6)$$

The parameters of the potentials for the ^{14}C+^{11}B and ^{15}C+^{10}B interactions, taken from global systematics [13] and used in our calculations, are listed in Table III. The parameter $r_C = 1.556$ fm was used for both reaction channels [13].

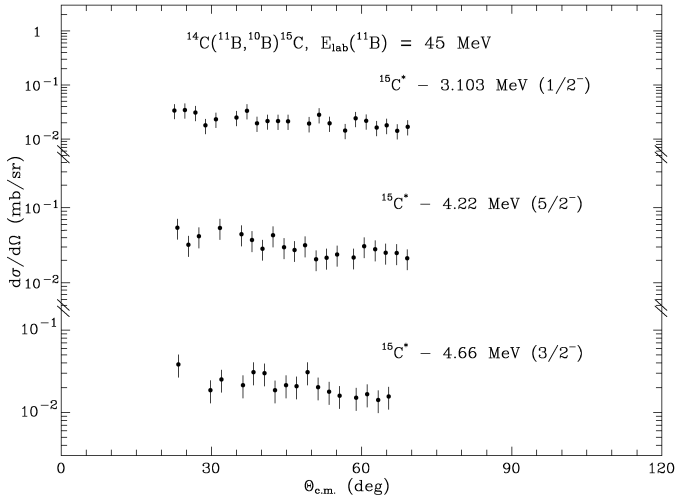

Fig. 7. Angular distributions of the ^{14}C(^{11}B,^{10}B)^{15}C reaction for the excited 3.103 MeV ($1/2^-$), 4.22 MeV ($5/2^-$) and 4.66 MeV ($3/2^-$) states of ^{15}C.

TABLE III

Parameters of the global OM potentials from Ref. [13] — original (a), (c) and modified (b), (d).

T+P	V_0 [MeV]	r_V [fm]	a_V [fm]	W_S [MeV]	r_W [fm]	a_W [fm]	W_D [MeV]	r_D [fm]	a_D [fm]	Pot.
^{14}C+^{11}B	258.14	1.266	0.726	15.84	1.640	0.600	45.52	1.200	0.843	(a)
^{14}C+^{11}B	258.14	1.566	0.726	13.34	1.940	0.900				(b)
^{15}C+^{10}B	263.02	1.267	0.726	10.10	1.640	0.600	49.03	1.200	0.843	(c)
^{15}C+^{10}B	263.02	1.317	0.726	10.10	1.640	0.800				(d)

As mentioned by the authors of [13], their global OM potentials describe the experimental data for ^{8,10,11}B elastic scattering from heavier targets (from ^{27}Al to ^{209}Bi) much better than from lighter ($A < 27$) targets. However, it is an interesting exercise to test this global potential systematics for the lighter system as studied here. The potential for the ^{11}B+^{14}C elastic scattering at $E_{\rm lab}(^{11}{\rm B}) = 45$ MeV was generated (see Table III) and compared to the data as shown by the long-dashed curve (pot. (a)) in Fig. 8. As expected, the potential scattering cross sections go well below the experimental data for $\theta_{\rm cm} > 55^\circ$ even with the inclusion of the ground-state reorientation of ^{11}B which is the main inelastic process affecting the ^{11}B+^{14}C elastic scattering cross sections [15], as shown by the short-dashed curve (pot. (a)+reor. ^{11}B). Besides that, diffraction phase disagreement is observed at forward angles between the experimental data and calculations. In order to improve the fit, we searched for the OM potential parameters that affected significantly the results of calculations and found that the contribution of the strong absorption by the surface imaginary potential $W_D(r)$ generates the resulting cross sections that are several orders of magnitude lower than the experimental data in the middle and backward angle regions. Thus, omitting the surface part of the global OMP and slightly changing the parameters of the real and imaginary parts of volume potentials, we could reach a good agreement with the experimental data as presented in Fig. 8 by the dot-dashed curve showing the results of calculations for potential scattering with modified global OM parameters (pot. (b)) and the solid curve showing the coherent sum of this potential scattering and ^{11}B reorientation.

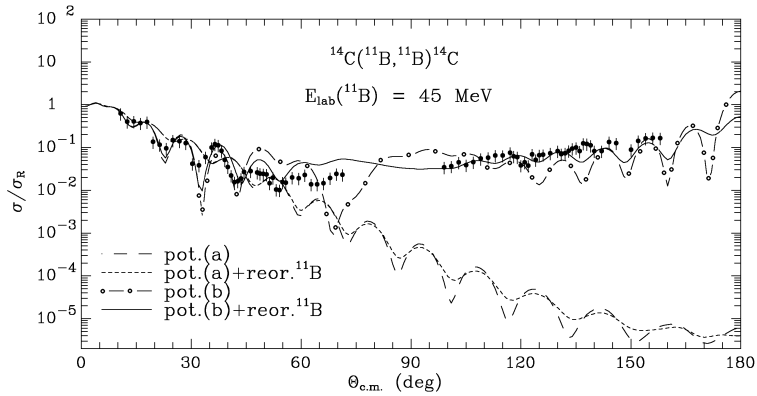

Fig. 8. Angular distributions for ^{14}C(^{11}B,^{11}B)^{14}C elastic scattering. The curves show results of calculations with the potential parameters listed in Table III (see the text and the figure captions for details).

The short-dashed curve in Fig. 9, which lies below the experimental data, shows the calculated cross sections for the direct transfer of a neutron in the ^{14}C(^{11}B,^{10}B)^{15}C reaction with the original global OM potentials (Table III) used for the entrance (pot. (a)) and exit (pot. (c)) channels. Using the parameters of the modified OMP for the entrance channel (pot. (b)) but original parameters [13] for the exit reaction channel (pot. (c)) does not lead to the improvement of the reaction data fit as shown in Fig. 9 by the long-dashed curve (pot. (b)+(c)). If for the exit reaction channel the surface imaginary potential is omitted, and the parameters of radius for real and diffuseness for imaginary volume potentials are slightly increased, the reasonable agreement with the experimental data is obtained as shown in Fig. 9 by the solid curve (pot. (b)+(d)).

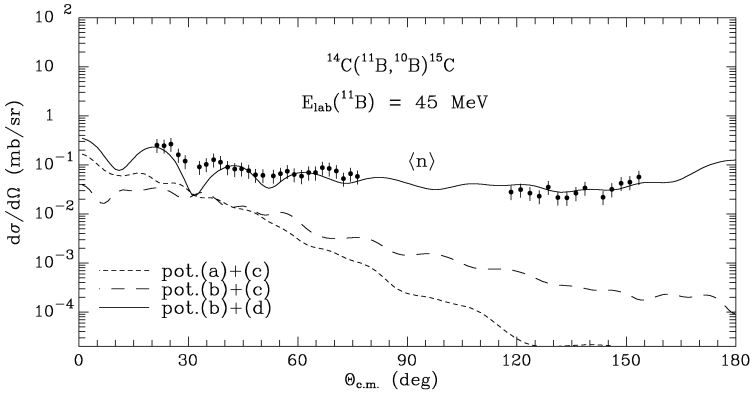

Fig. 9. Angular distributions of the ^{14}C(^{11}B,^{10}B)^{15}C reaction for the ground states of ^{10}B and ^{15}C. The curves show CRC cross sections for the transfer of a neutron, calculated with different OM potentials from Table III (see the text and the figure captions for details).

On the left-hand side of Fig. 10, the comparison of the real volume potentials $V_0(r)$ from Table III for ^{14}C+^{11}B interaction — original as generated from paper [13] and modified in this work are shown by the thin ((a) — V_0) and thick ((b) — V_0) solid curves, respectively, the sum of the volume and surface imaginary potentials from [13] is shown by the thin dashed curve ((a) — W_S+W_D) and modified imaginary potential is shown by the thick dashed curve ((b) — W_S). Thus weaker absorption by the modified imaginary potential in the interaction region (4–7 fm) is leading to the increase of the calculated cross sections for the middle and backward angles (Fig. 8). The potentials of the same kind for ^{15}C+^{10}B interaction are shown in the middle of Fig. 10, and, the same as for the elastic ^{11}B+^{14}C scattering, weaker absorption by the modified imaginary potential leads to a good agreement of the calculations with the experimental data (solid curve in Fig. 9). The

comparison of real and imaginary parts of volume potentials for ^{15}C+^{10}B interaction, deduced in this paper (Table II) and modified (pot. (d) in Table III) are shown by the solid and dashed curves, respectively, on the right-hand side of Fig. 10. Their difference in the interaction region (4–7 fm) is not large, so the results of calculations for the transfer of a neutron in the ^{14}C(^{11}B,^{10}B)^{15}C reaction are slightly different (see solid curves in Figs. 3 and 9), but both calculations reproduce the experimental data reasonably well.

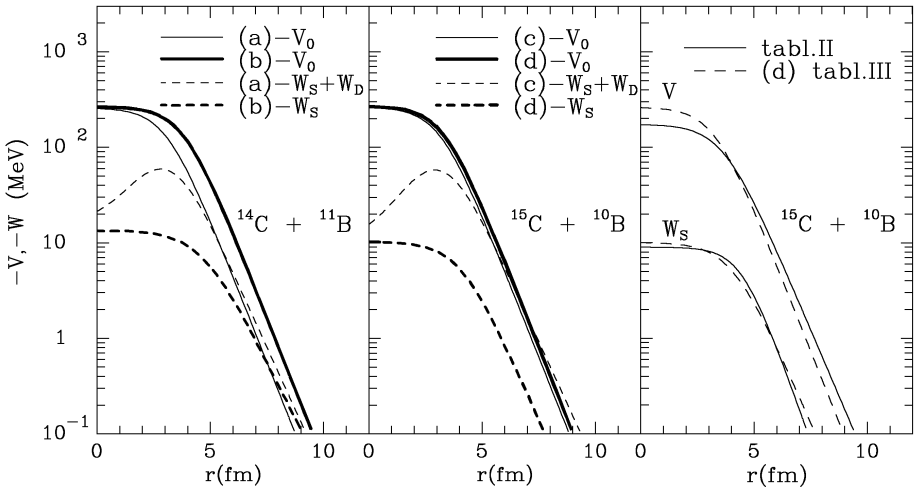

Fig. 10. Radial dependence of OM potentials for ^{14}C+^{11}B (left-hand side) and ^{15}C+^{10}B (middle) interaction, calculated using parameters from Table III. For ^{15}C+^{10}B interaction (right-hand side of the figure) the parameters were taken from Tables II and III (see the text and the figure captions for details).

In summary, the calculations performed for ^{11}B+^{14}C elastic scattering and one-neutron transfer reaction, ^{14}C(^{11}B,^{10}B)^{15}C, with the global potentials from [13], can describe the experimental data providing that their imaginary parts are strongly reduced at the surface. This indicates that some coupled channels effects, not included in the analysis, are playing an important role. Thus, in order to improve the fit to the experimental data of ^{8,10,11}B elastic scattering from some light ($A < 27$) targets [13], the mechanisms of anomalous large angle scattering (ALAS) must be carefully studied.

4. Summary and conclusions

New experimental data for differential cross sections of the ^{14}C(^{11}B,^{10}B)^{15}C reaction at $E_{\rm lab}(^{11}\mathrm{B})$ = 45 MeV were obtained for the ground states of ^{10}B and ^{15}C, as well as for the excited 0.72 MeV (1^+) of

^{10}B + 0.74 MeV ($5/2^+$) states of ^{15}C (unresolved in the experiment), the 1.74 MeV (0^+), 2.154 MeV (1^+), 3.587 MeV (2^+) states of ^{10}B and the 3.103 MeV ($1/2^-$), 4.22 MeV ($5/2^-$), 4.66 MeV ($3/2^-$) states of ^{15}C. The experimental data, excluding those for reactions leading to the ^{15}C excited states above the neutron-binding energy, were analyzed within the coupled reaction channels method that included the elastic and inelastic scattering channels of ^{11}B+^{14}C as well as one- and two-step transfers in the coupling scheme. For the excited states of ^{15}C placed above the threshold of neutron emission (S_n = 1.218 MeV), CRC calculations will be presented in a separate paper.

For the entrance reaction channel, a Woods–Saxon potential was used with the parameters deduced from a previous analysis of the experimental data for the ^{11}B+^{14}C elastic scattering at $E_{\rm lab}(^{11}{\rm B})$ = 45 MeV [15]. Spectroscopic amplitudes for nucleons and clusters, needed for the calculations of the reaction cross sections, were obtained within the translational-invariant shell model [17] by means of the computer code DESNA [18]. The spectroscopic factors of nucleons and clusters in nuclei are defined by the squares of these spectroscopic amplitudes.

The present analysis of the experimental data for the ^{14}C(^{11}B, ^{10}B)^{15}C reaction found that direct neutron transfer dominates over the whole angular range for transitions to the ground and excited states of ^{10}B, while contributions of two-step transfers of nucleons and clusters are negligible.

From the analysis, OM potential for the exit channel, ^{10}B+^{15}C, was derived. The comparison of this potential with the potential for the system ^{10}B+^{12}C [12] has shown that the potential for ^{15}C is more diffuse at the surface. Moreover, calculations for the ^{14}C(^{11}B,^{10}B)^{15}C$_{\rm gs}$ reaction with the use of ^{10}B+^{12,13,15}C OM potentials in the exit reaction channel generated very different results that might be due to different internal structure of these carbon isotopes.

The experimental data for the ^{11}B+^{14}C elastic scattering and for one-neutron transfer reaction, ^{14}C(^{11}B,^{10}B)^{15}C$_{\rm gs}$, could be reproduced by the OM and CRC calculations using the parameters of the global phenomenological OM potential for ^{8,10,11}B projectiles proposed in Ref. [13], only when the surface imaginary terms were omitted, with some slight change of the other parameters. This suggests that some coupled channels effects, not included in the analysis, are playing a role. Thus, an investigation of ALAS mechanism for processes induced by boron isotopes from various light targets is of importance.

REFERENCES

[1] T. Malkiewicz *et al.*, «Production of a ^{15}C radioactive ion beam based on $^{18}O(n,\alpha)$», *Eur. Phys. J. A* **55**, 88 (2019).

[2] Y.Z. Sun *et al.*, «Two-neutron removal cross sections from ^{15,16}C at around 240 MeV/nucleon», *Phys. Rev. C* **99**, 024605 (2019).

[3] S. Bedoor *et al.*, «Structure of ^{14}C and ^{14}B from the $^{14,15}C(d,^3He)^{13,14}B$ reactions», *Phys. Rev. C* **93**, 044323 (2016).

[4] H.G. Bohlen *et al.*, «Structure of neutron-rich Be and C isotopes», *Phys. Atom. Nucl.* **66**, 1494 (2003).

[5] M. McCleskey *et al.*, «Determination of the asymptotic normalization coefficients for $^{14}C + n \leftrightarrow ^{15}C$, the $^{14}C(n,\gamma)^{15}C$ reaction rate, and evaluation of a new method to determine spectroscopic factors», *Phys. Rev. C* **89**, 044605 (2014).

[6] D.Y. Pang, A.M. Mukhamedzhanov, «Asymptotic normalization coefficients and spectroscopic factors from deuteron stripping reactions», *Phys. Rev. C* **90**, 044611 (2014).

[7] A.M. Mukhamedzhanov *et al.*, «Asymptotic normalization coefficients from the $^{14}C(d,p)^{15}C$ reaction», *Phys. Rev. C* **84**, 024616 (2011).

[8] A.N. Abdullah, «Investigation of halo structure of neutron rich ^{14}B, ^{15}C, ^{19}C and ^{22}N nuclei in the two body model», *Int. J. Mod. Phys. E* **29**, 2050015 (2020).

[9] D. Carbone *et al.*, «Microscopic cluster model for the description of new experimental results on the $^{13}C(^{18}O,^{16}O)^{15}C$ two-neutron transfer at 84 MeV incident energy», *Phys. Rev. C* **95**, 034603 (2017).

[10] D. Carbone *et al.*, «Microscopic Cluster Model for the Description of (^{18}O,^{16}O) Two-neutron Transfer Reactions», *Acta Phys. Pol. B* **49**, 373 (2018).

[11] J.F. Mateja *et al.*, «^{11}B+^{12}C and ^{10}B+^{13}C fusion cross sections», *Phys. Rev. C* **25**, 2963 (1982).

[12] N. Burtebayev *et al.*, «Measurement and analysis of ^{10}B+^{12}C elastic scattering at energy of 41.3 MeV», *Int. J. Mod. Phys. E* **28**, 1950028 (2019).

[13] Yong-Li Xu *et al.*, «Applicability of ^{9}Be global optical potential to description of ^{8,10,11}B elastic scattering», *Chin. Phys. C* **44**, 034101 (2020).

[14] S.Yu. Mezhevych *et al.*, «The ^{13}C+^{11}B elastic and inelastic scattering and isotopic effects in the ^{12,13}C+^{11}B scattering», *Nucl. Phys. A* **724**, 29 (2003).

[15] S.Yu. Mezhevych *et al.*, «Elastic and inelastic scattering of ^{14}C+^{11}B *versus* ^{12,13}C+^{11}B», *Eur. Phys. J. A* **50**, 4 (2014).

[16] S.Yu. Mezhevych *et al.*, «$^{13}C(^{11}B,\ ^{12}C)^{12}B$ Reaction at 45 MeV, ^{12}C + ^{12}B Interaction *Versus* that of ^{12}C + ^{10,11}B», *Acta Phys. Pol. B* **51**, 1949 (2020).

[17] Yu.F. Smirnov, Yu.M. Tchuvilsky, «Cluster spectroscopic factors for the p-shell nuclei», *Phys. Rev. C* **15**, 84 (1977).

[18] A.T. Rudchik, Yu.M. Tchuvilsky, The Code DESNA, report KIYAI-82-12 Kiev Institute for Nuclear Researches, 1982.

[19] A.T. Rudchik, Yu.M. Tchuvilsky, *Ukr. Fiz. Zh.* **30**, 819 (1985).

[20] A.N. Boyarkina, «Structure of the 1p-shell nuclei», Report, Moscow State University, 1973.

[21] I.J. Thompson, «Coupled reaction channels calculations in nuclear physics», *Comp. Phys. Rep.* **7**, 167 (1988).

[22] M.N. El-Hammamy, A. Attia, F.A. El-Akkad, A.M. Abdel-Moneim, «Study of ^{3}He inelastic scattering on ^{13}C and ^{14}C at 37.9 MeV», *Chin. Phys. C* **38**, 034102 (2014).

[23] S.Yu. Mezhevych *et al.*, «Excitation of ^{14}C by 45 MeV ^{11}B ions», *Nucl. Phys. A* **753**, 13 (2005).